Electronic Supplementary Information (ESI)

Post-Deposition In-Situ Passivation of $AgBiS_2$ Nanocrystal Inks for High-Efficiency Ultra-Thin Solar Cells

Jae Taek Oh,[a] Yongjie Wang,[a] Carmelita Rodà,[a] Debranjan Mandal,[a] Gaurav Kumar,[a] Guy Luke Whitworth,[a] Gerasimos Konstantatos*[ab]

[a]ICFO–Insitut de Ciències Fotòniques, The Barcelona Institute of Science and Technology, Castelldefels, Barcelona, 08860, Spain
E-mail: Gerasimos.konstantatos@icfo.eu

[b]ICREA–Institució Catalana de Recerca i Estudiats Avançats, Lluis Companys 23, Barcelona, 08010, Spain

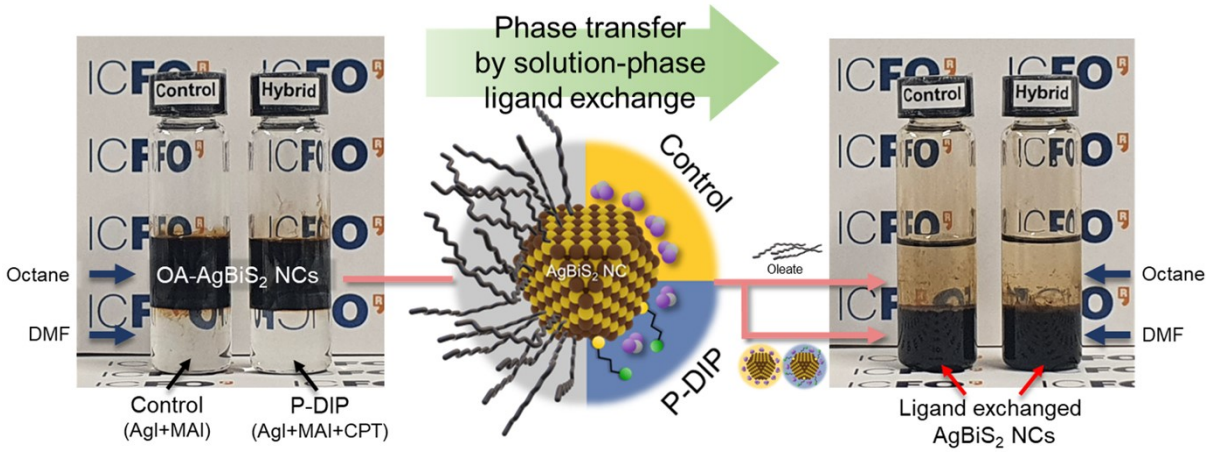

Fig. S1 Photographs and schematics of solution-phase ligand-exchange-based $AgBiS_2$ NCs ink fabrication process. After vigorous mixing, oleate capped (OA-) $AgBiS_2$ NCs were transferred from octane to DMF phase by ligand-exchange.

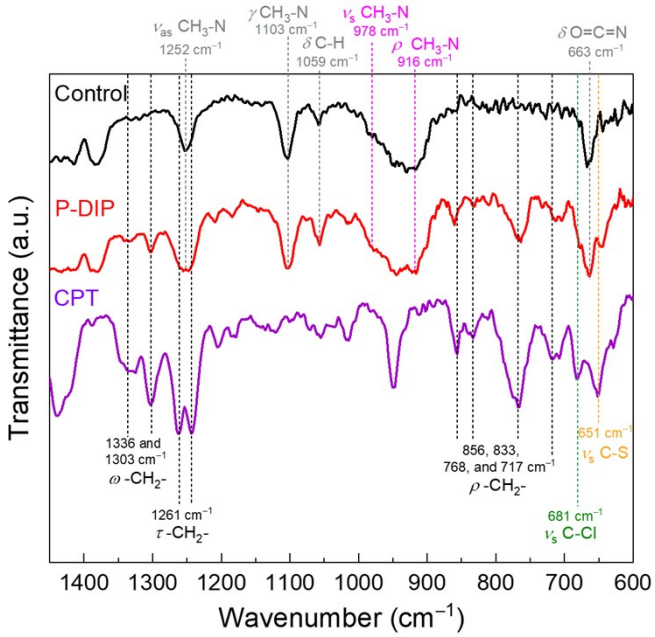

Fig. S2 FTIR spectra of Control (black), P-DIP (red), and CPT-exchanged (purple) $AgBiS_2$ NCs ink powders in the fingerprint (1400–600 cm^{-1}) region. Symbols of ν_s, ν_{as}, δ, ρ, τ, and ω represent vibrational modes of symmetric, asymmetric stretches, bending, rocking, twisting, and wagging respectively[1,2]. Peaks marked in grey and magenta letters were derived from remaining DMF[3] and methylammonium[4] in $AgBiS_2$ NCs ink powders, respectively.

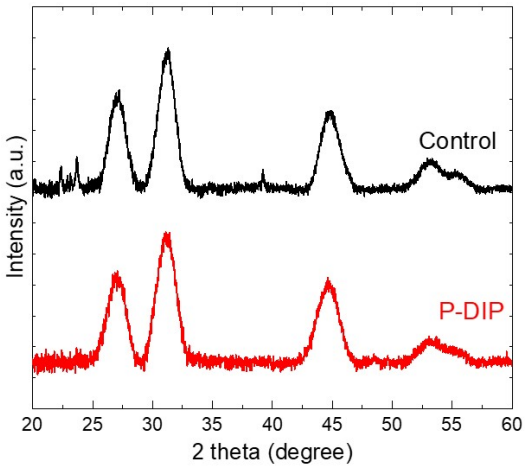

Fig. S3 XRD patterns of as-prepared Control and P-DIP $AgBiS_2$ NCs ink powders.

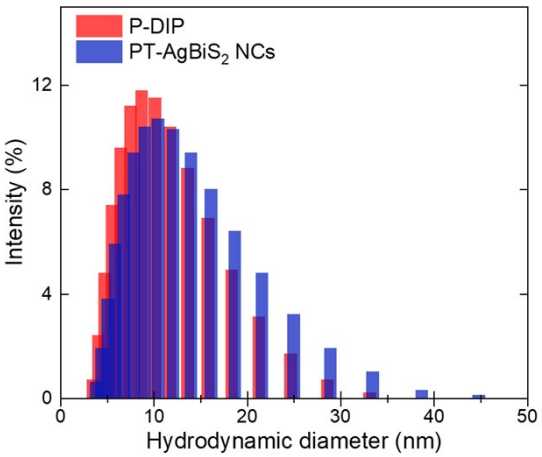

Fig. S4 DLS analysis of $AgBiS_2$ NCs solution dispersed in DMF, where 1-propanethiol (PT) was used as an additive instead of CPT, denoted as PT-$AgBiS_2$ NCs. PT-$AgBiS_2$ NCs have slightly larger D_h in DMF solution than those of P-DIP, indicating the presence of more aggregated and/or agglomerated colloidal $AgBiS_2$ NCs. This demonstrates that not only steric stabilization by alkyl chain, but also the polar C–Cl tail in CPT are important for enhancing the colloidal dispersibility of $AgBiS_2$ NCs ink. Device performance of PT-$AgBiS_2$ NCs ink solar cell is summarized in **Fig. S17**.

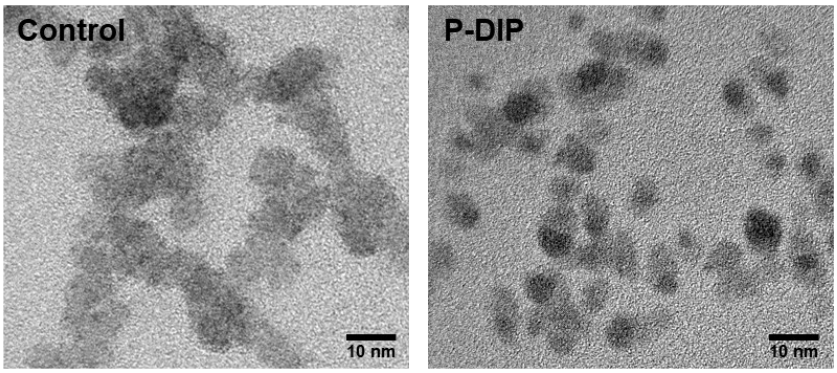

Fig. S5 TEM images of as prepared Control (left) and P-DIP (right) $AgBiS_2$ NCs inks after solution-phase ligand-exchange process.

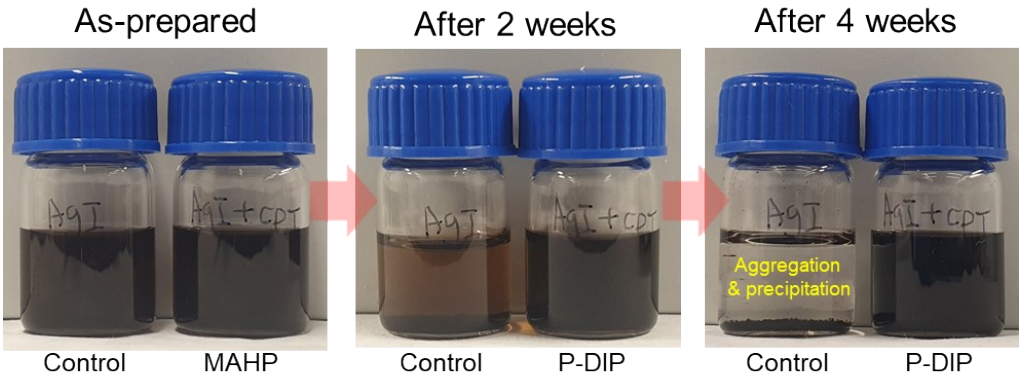

Fig. S6 Temporal colloidal stability test. Photograph shows Control and P-DIP $AgBiS_2$ NCs solutions in DMF according to the storage time. Within 2 weeks, Control $AgBiS_2$ NCs (left vial) started aggregating and completely precipitated in 4 weeks, while no aggregation or precipitation was observed in the P-DIP $AgBiS_2$ NCs solution (right vial).

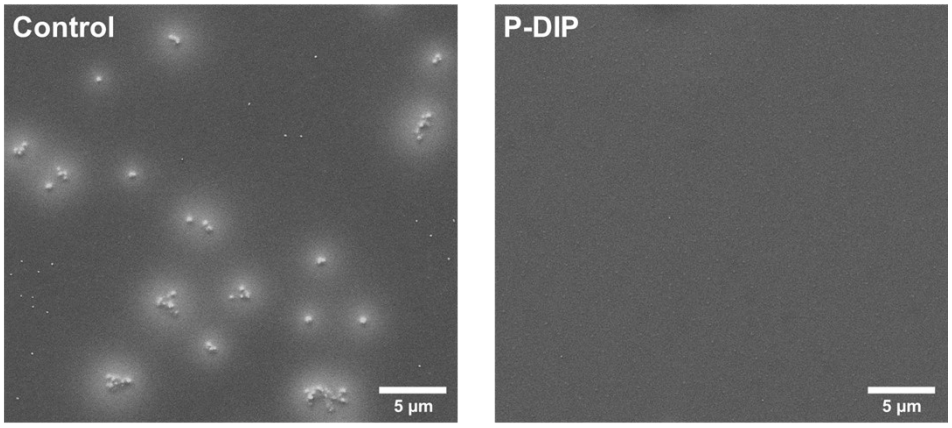

Fig. S7 SEM images captured from a top-view perspective of Control and P-DIP $AgBiS_2$ NCs ink films. A smoother and improved surface morphology was observed in the P-DIP $AgBiS_2$ NCs ink film.

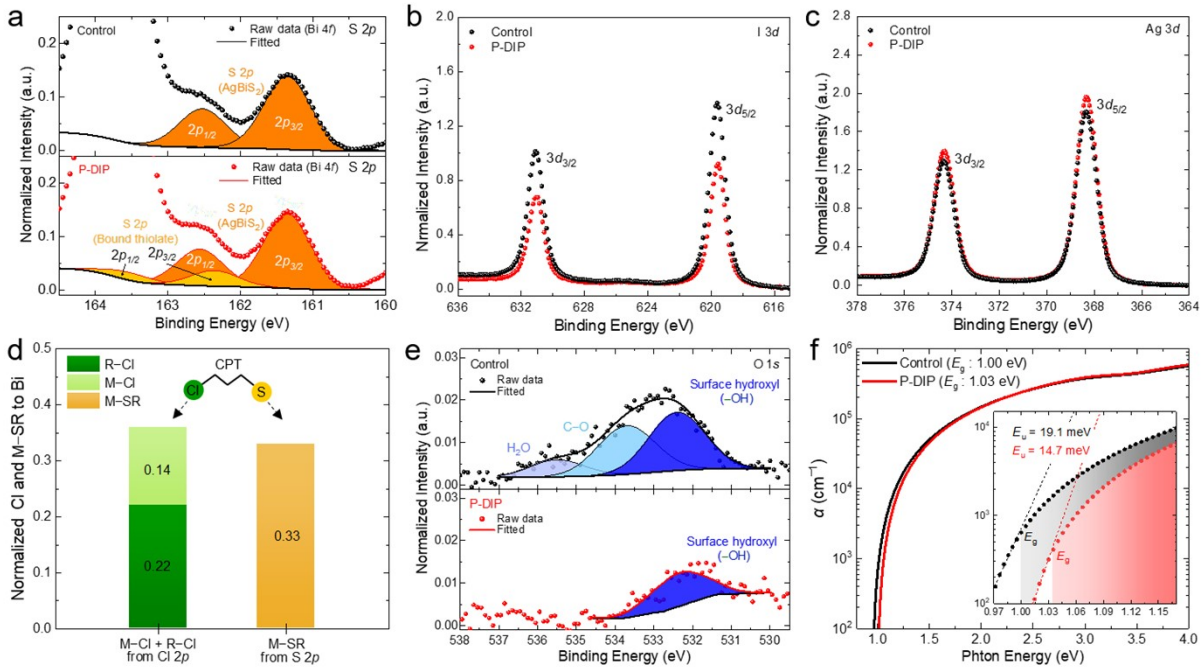

Fig. S8 Improved passivation on P-DIP $AgBiS_2$ NCs. XPS core-level spectra of Control and P-DIP $AgBiS_2$ NCs ink films after annealing at the optimized temperature of 150 °C (a–c and e). All XPS spectra were normalized to Bi. (a) S 2*p*, enlarged from Bi 4*f* spectra. Each component is shaded as $AgBiS_2$ in orange, and bound thiolate (M–SR) in yellow. (b) I 3*d*, and (c) Ag 3*d*, respectively. (d) Relative amounts of Cl (i.e. M–Cl + R–Cl) and M–SR, calculated separately using relative area of each component in Cl 2*p* and S 2*p* XPS spectra (**Table S2** and **S3**) and relative amounts of Cl and S of P-DIP ink film (**Table 1**). (e) O 1s spectra of Control and P-DIP ink films. Each component is shaded as follows: –OH in blue, C–O in sky blue, and H_2O in light blue. (f) Absorption coefficient (α) of Control and P-DIP ink films measured by ellipsometry techniques. The band gap (E_g) of each film were obtained from Tauc plots, as presented in **Fig. S12**. The inset shows the enlarged spectra near the E_g of each $AgBiS_2$ NCs ink film aimed at defining E_u, which was confirmed as 19.1 and 14.7 meV for Control and P-DIP ink films, respectively.

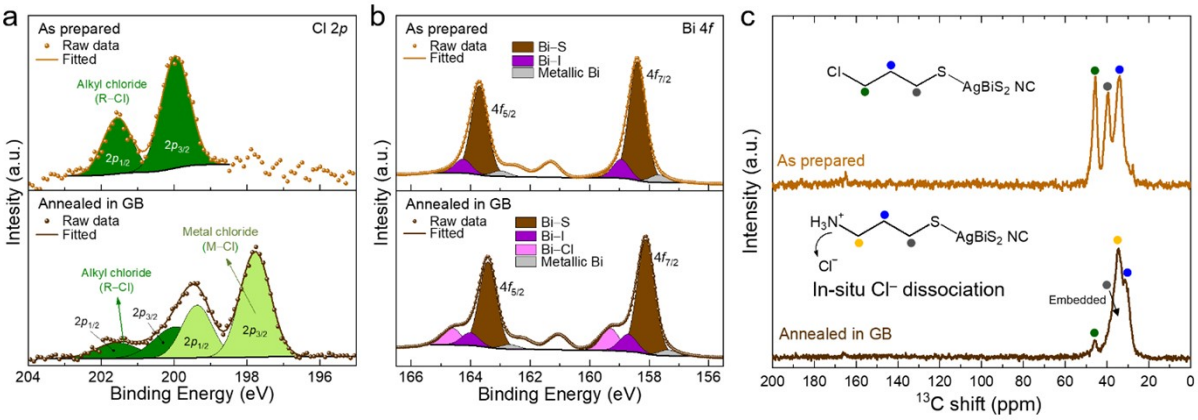

Fig. S9 Mild annealing induced in-situ passivation on P-DIP $AgBiS_2$ NCs film. XPS core-level spectra of as prepared (in light brown) and annealed (in dark brown) P-DIP $AgBiS_2$ NCs ink films. (a) Cl 2*p*, and (b) Bi 4*f* spectra. (c) ^{13}C solid-state NMR spectra of as prepared and annealed P-DIP $AgBiS_2$ NCs ink powder (see **Note S1**).

Note S1

To investigate mild annealing induced in-situ passivation, we conducted XPS measurements on both as prepared and annealed P-DIP $AgBiS_2$ NCs films at 150 °C in the glove box with longer annealing time and 40 mM of CPT (optimized conditions for the solar cell is 30 sec and 10 mM, respectively) to acquire adequate signals. As shown in **Fig. S9a**, the Cl 2*p* XPS spectra of as prepared film present only R–Cl component corresponding to CPT, suggesting that activation energy barrier for C–Cl bond cleavage could not be suppressed at room temperature. Following annealing, there was the emergence of M–Cl component alongside the reduced that of R–Cl, indicating the mild annealing induced dissociation of Cl^- ions. Simultaneously, Bi–Cl component at the higher binding energy was observed in Bi 4*f* XPS spectra (**Fig. S9b**), indicating improved passivation on P-DIP $AgBiS_2$ NCs[5] by dissociated Cl^- ions. Furthermore, Bi 4*f* spectra was shifted to lower binding energy (~0.3 eV). This change corresponds to the cation homogenization of $AgBiS_2$ NCs[6]. To identify the mechanism of Cl^- dissociation, we further performed the ^{13}C solid-state nuclear magnetic resonance (NMR) experiments on as prepared and annealed P-DIP ink powders. We observed that the peak intensity of α-carbon adjacent to chlorine (45.6 ppm; olive dot) significantly reduced after mild annealing and the peak corresponding to alkyl ammonium[7,8] (34.6 ppm; yellow dot) simultaneously emerged, indicating the replacement of Cl with amine species. Considering that the degradation of DMF

produces amine derivatives, and this reaction is further accelerated by an increase in temperature[9], we speculated that these generated amine derivatives during mild annealing substitute the Cl resulting in the formation of ammonium cation. Given that the C–Cl bond in acyl chloride can be catalytically cleaved by Ag[10] upon mild annealing, Cl in CPT may interact with surface-exposed Ag in as prepared P-DIP $AgBiS_2$ NCs and subsequent mild annealing potentially initiate the C–Cl bond cleavage trough overcoming the activation energy barrier. This can be followed by the addition of amine derivatives to the resulting carbocation sites.

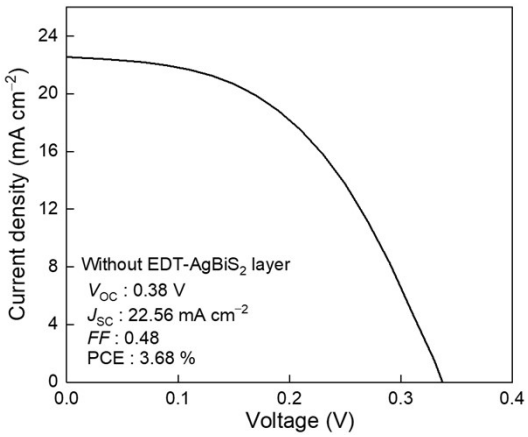

Fig. S10 Device performance of P-DIP $AgBiS_2$ NCs ink solar cell without EDT-$AgBiS_2$ NCs layer. V_{OC} and *FF* were significantly dropped in the device without EDT-$AgBiS_2$ layer, indicating severe charge recombination occurred at the interface. Energy-level-diagram (**Fig. 2c**) shows the energy level difference between PTAA and $AgBiS_2$ NCs ink layer could be reduced from 0.37 to 0.22 eV by introducing EDT-$AgBiS_2$ layer. This could mitigate the interface recombination caused by energy-level mismatch between $AgBiS_2$ NCs ink and PTAA layers, thereby facilitating hole transport at the interface.

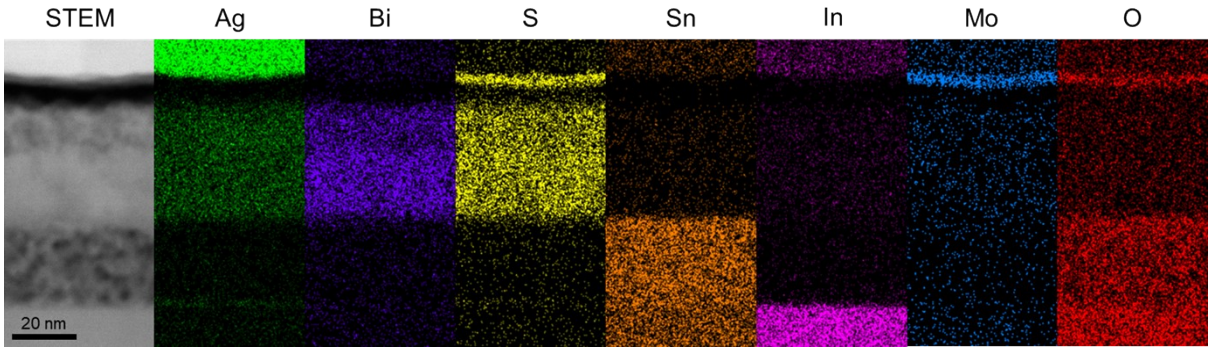

Fig. S11 EDX elemental mapping on cross-TEM image of P-DIP $AgBiS_2$ NCs ink solar cell. The sulphur contents were observed in MoO_3 layer because energy values of emitted X-ray from S Kα (2.307 KeV) and Mo Lα (2.293 KeV) were overlapped in the EDX spectrum.

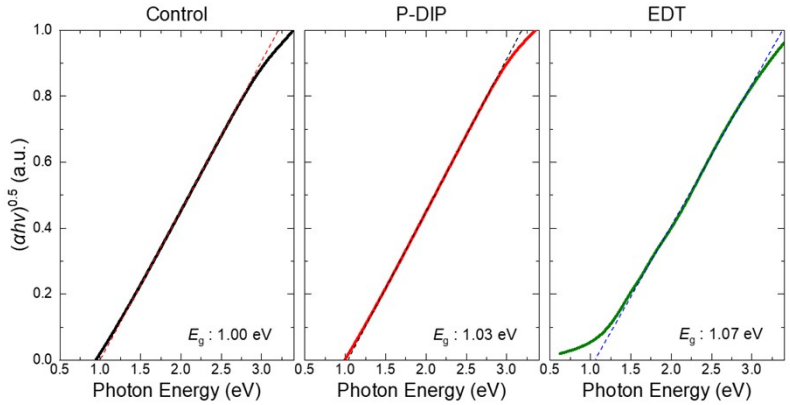

Fig. S12 Band gap determination of Control, P-DIP, EDT-exchanged $AgBiS_2$ NCs films. Tauc plots are plotted using α obtained from ellipsometry measurements. Control and P-DIP $AgBiS_2$ NCs films were annealed at 150 °C, and EDT-$AgBiS_2$ NCs film was annealed at 80 °C according to the device optimization conditions.

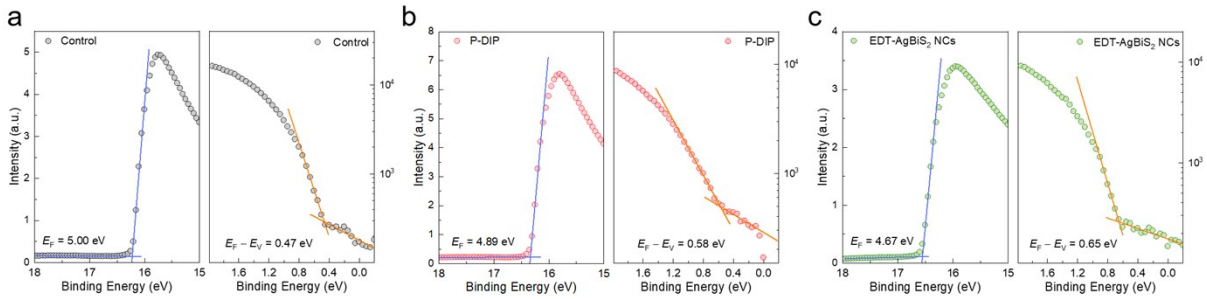

Fig. S13 UPS spectra. Fermi-level region (left), and Secondary cut-off region (right) of (a) Control (b) P-DIP $AgBiS_2$ NCs ink, and (c) EDT-exchanged $AgBiS_2$ NCs films. Samples are annealed at 150 °C for Control and P-DIP $AgBiS_2$ NCs ink films and 80 °C for EDT-$AgBiS_2$ NCs film. The EDT-$AgBiS_2$ NCs film was prepared on the $AgBiS_2$ NCs ink film.

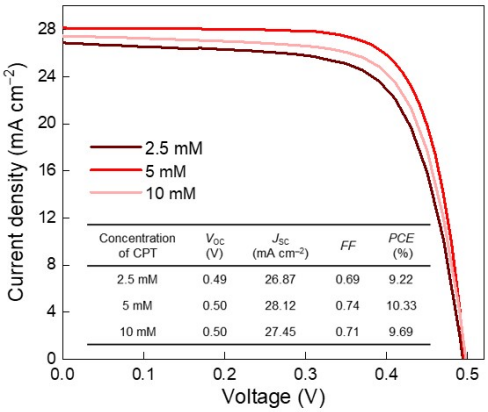

Concentration of CPT	V_{OC} (V)	J_{SC} (mA cm^{-2})	*FF*	*PCE* (%)
2.5 mM	0.49	26.87	0.69	9.22
5 mM	0.50	28.12	0.74	10.33
10 mM	0.50	27.45	0.71	9.69

Fig. S14 Device performance of P-DIP $AgBiS_2$ NCs ink devices under varying different concentration of CPT. *J–V* curves and corresponding device parameters (the inset table) indicate that the optimized concentration of CPT as an additive is 5 mM in AgI+MAI pre-dissolved DMF ligand solution. All P-DIP $AgBiS_2$ NCs ink films were annealed at 150 °C after film formation following the optimized annealing condition detailed in **Fig. S15** and **Note S2**.

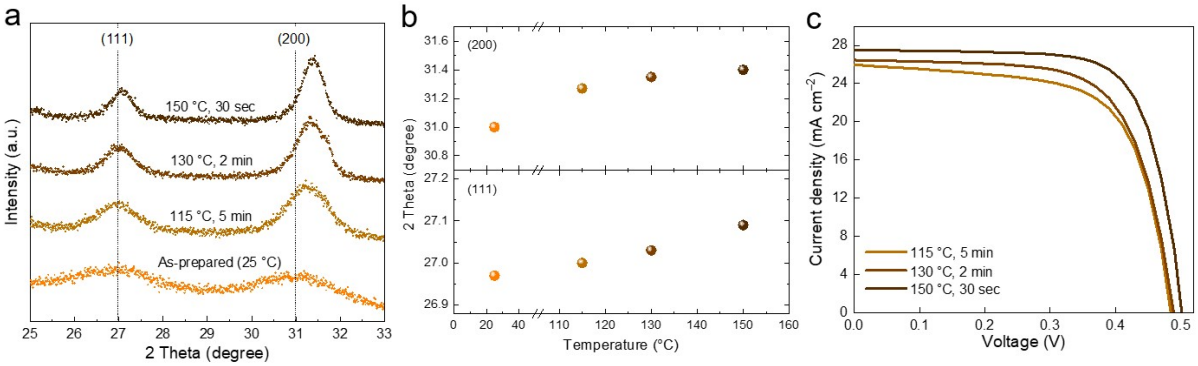

Fig. S15 Cation disordering homogenization of P-DIP $AgBiS_2$ NCs films under various annealing temperature. (a) XRD spectra and (b) corresponding variation of 2 theta values of P-DIP $AgBiS_2$ NCs ink films. (c), *J–V* curves of corresponding P-DIP $AgBiS_2$ NCs ink devices. Device parameters are summarized in **Table S6** (see **Note S2).**

Note S2

The cation disordering homogenization of P-DIP ink films was identified with XRD measurements. As shown in **Fig. S15a** and **b**, the peak positions corresponding to (111) and (200) planes of P-DIP $AgBiS_2$ NCs were gradually shifted to higher angles with increasing annealing temperature and optimized time, this shift demonstrates the reduction in interplanar distance mainly due to the shortening of the Ag–S bond lengths. Furthermore, the sharpening of XRD peaks is also observed with an increase in annealing temperature, indicating the improved crystallinity of $AgBiS_2$ NCs due to constrained bond length distributions and decreased octahedral distortion through the cationic homogenization[6]. The P-DIP $AgBiS_2$ NCs annealed at 150 °C shows the biggest shift of peak position and narrowest peak shape among samples, suggesting that higher temperature can induce better cationic homogenization on $AgBiS_2$ NCs leading to reduced trap density and absorption ability in $AgBiS_2$ NCs films. Corresponding device performances according to the different annealing temperature on P-DIP $AgBiS_2$ NCs films proved that P-DIP ink device annealed at 150 °C exhibited the highest *PCE* of 9.98% compared to those of annealed at lower temperature (**Fig. S15c** and **Table S6**), which is coincident with XRD spectra.

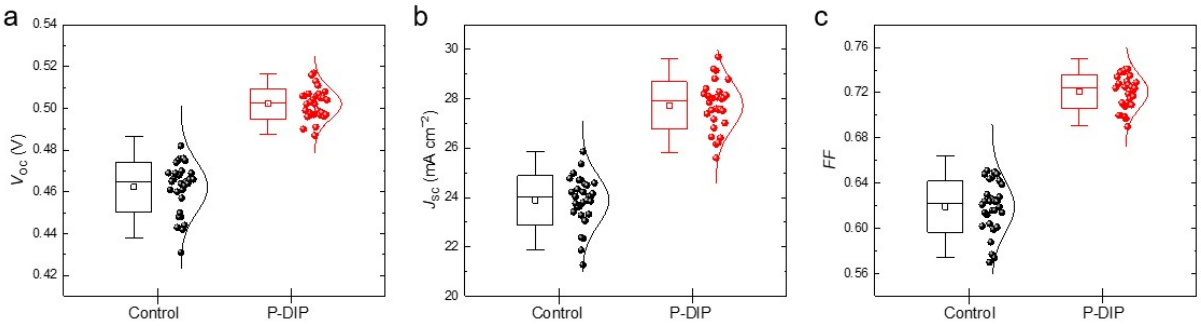

Fig. S16 Device histogram of Control (black) and P-DIP (red) $AgBiS_2$ NCs ink solar cells. (a) V_{OC}. (b) J_{SC}. (c) *FF*, respectively. Each value was recorded from 30 different devices.

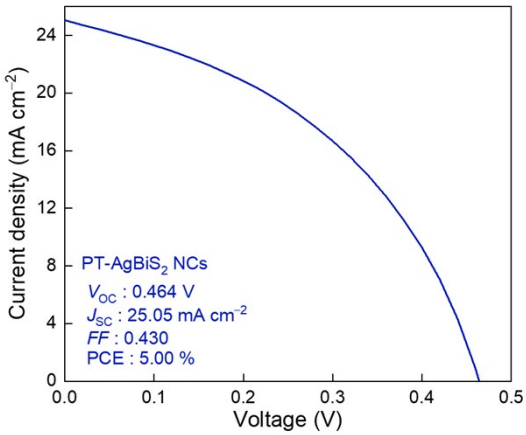

Fig. S17 Device performance of PT-$AgBiS_2$ NCs ink solar cell. Reduced photovoltaic performance was observed in PT-$AgBiS_2$ NCs ink device, suggesting the importance of Cl in passivating the $AgBiS_2$ NCs surfaces.

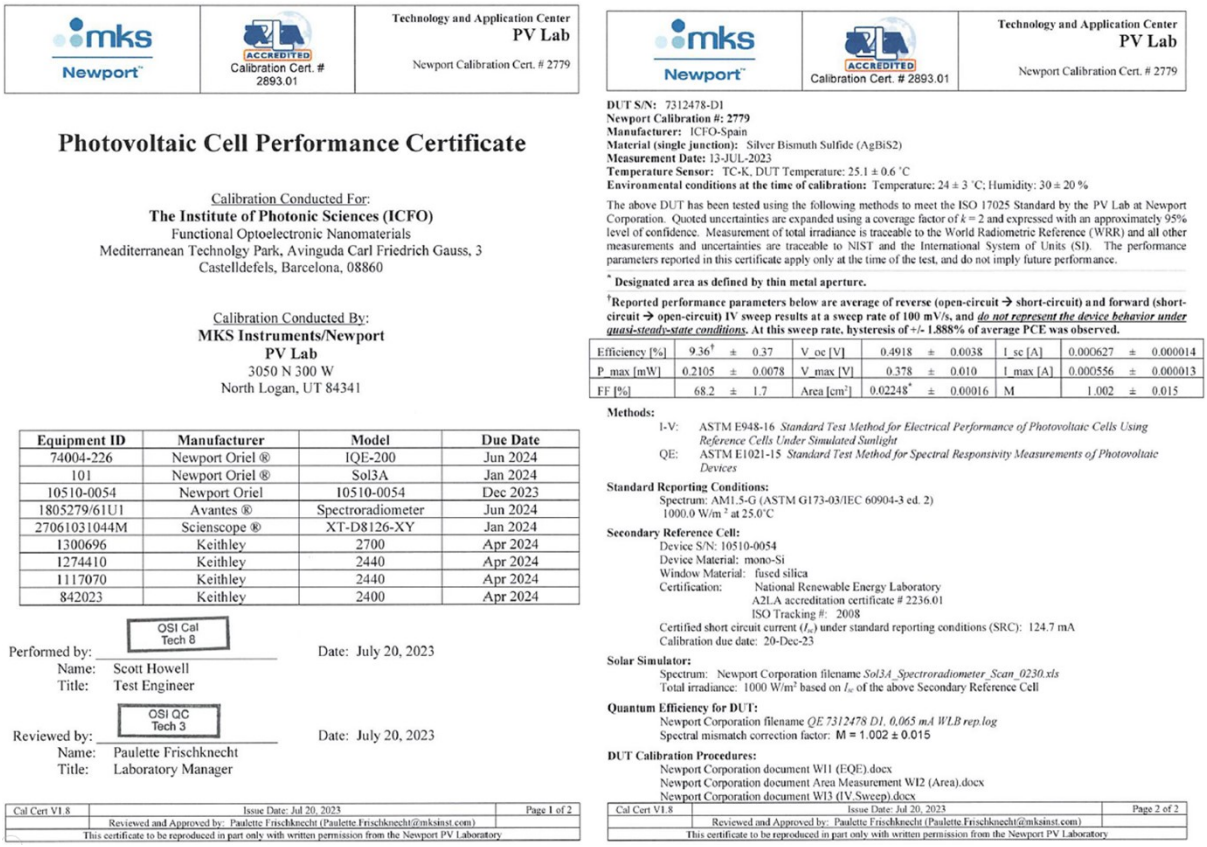

mks Newport

ACCREDITED Calibration Cert. # 2893.01

Technology and Application Center
PV Lab
Newport Calibration Cert. # 2779

Photovoltaic Cell Performance Certificate

Calibration Conducted For:
The Institute of Photonic Sciences (ICFO)
Functional Optoelectronic Nanomaterials
Mediterranean Technolgy Park, Avinguda Carl Friedrich Gauss, 3
Castelldefels, Barcelona, 08860

Calibration Conducted By:
MKS Instruments/Newport
PV Lab
3050 N 300 W
North Logan, UT 84341

Equipment ID	Manufacturer	Model	Due Date
74004-226	Newport Oriel ®	IQE-200	Jun 2024
101	Newport Oriel ®	Sol3A	Jan 2024
10510-0054	Newport Oriel	10510-0054	Dec 2023
1805279/61U1	Avantes ®	Spectroradiometer	Jun 2024
27061031044M	Scienscope ®	XT-D8126-XY	Jan 2024
1300696	Keithley	2700	Apr 2024
1274410	Keithley	2440	Apr 2024
1117070	Keithley	2440	Apr 2024
842023	Keithley	2400	Apr 2024

Performed by: OSI Cal Tech 8 Date: July 20, 2023
Name: Scott Howell
Title: Test Engineer

Reviewed by: OSI QC Tech 3 Date: July 20, 2023
Name: Paulette Frischknecht
Title: Laboratory Manager

Cal Cert V1.8	Issue Date: Jul 20, 2023	Page 1 of 2
	Reviewed and Approved by: Paulette Frischknecht (Paulette.Frischknecht@mksinst.com)	
This certificate to be reproduced in part only with written permission from the Newport PV Laboratory		

mks Newport

ACCREDITED Calibration Cert. # 2893.01

Technology and Application Center
PV Lab
Newport Calibration Cert. # 2779

DUT S/N: 7312478-D1
Newport Calibration #: 2779
Manufacturer: ICFO-Spain
Material (single junction): Silver Bismuth Sulfide (AgBiS2)
Measurement Date: 13-JUL-2023
Temperature Sensor: TC-K, DUT Temperature: 25.1 ± 0.6 °C
Environmental conditions at the time of calibration: Temperature: 24 ± 3 °C; Humidity: 30 ± 20 %

The above DUT has been tested using the following methods to meet the ISO 17025 Standard by the PV Lab at Newport Corporation. Quoted uncertainties are expanded using a coverage factor of $k = 2$ and expressed with an approximately 95% level of confidence. Measurement of total irradiance is traceable to the World Radiometric Reference (WRR) and all other measurements and uncertainties are traceable to NIST and the International System of Units (SI). The performance parameters reported in this certificate apply only at the time of the test, and do not imply future performance.

* **Designated area as defined by thin metal aperture.**

† **Reported performance parameters below are average of reverse (open-circuit → short-circuit) and forward (short-circuit → open-circuit) IV sweep results at a sweep rate of 100 mV/s, and *do not represent the device behavior under quasi-steady-state conditions*. At this sweep rate, hysteresis of +/- 1.888% of average PCE was observed.**

Efficiency [%]	9.36†	±	0.37	V_oc [V]	0.4918	±	0.0038	I_sc [A]	0.000627	±	0.000014
P_max [mW]	0.2105	±	0.0078	V_max [V]	0.378	±	0.010	I_max [A]	0.000556	±	0.000013
FF [%]	68.2	±	1.7	Area [cm²]	0.0224*	±	0.00016	M	1.002	±	0.015

Methods:
I-V: ASTM E948-16 *Standard Test Method for Electrical Performance of Photovoltaic Cells Using Reference Cells Under Simulated Sunlight*
QE: ASTM E1021-15 *Standard Test Method for Spectral Responsivity Measurements of Photovoltaic Devices*

Standard Reporting Conditions:
Spectrum: AM1.5-G (ASTM G173-03/IEC 60904-3 ed. 2)
1000.0 W/m² at 25.0°C

Secondary Reference Cell:
Device S/N: 10510-0054
Device Material: mono-Si
Window Material: fused silica
Certification: National Renewable Energy Laboratory
A2LA accreditation certificate # 2236.01
ISO Tracking #: 2008
Certified short circuit current (I_{sc}) under standard reporting conditions (SRC): 124.7 mA
Calibration due date: 20-Dec-23

Solar Simulator:
Spectrum: Newport Corporation filename *Sol3A_Spectroradiometer_Scan_0230.xls*
Total irradiance: 1000 W/m² based on I_{sc} of the above Secondary Reference Cell

Quantum Efficiency for DUT:
Newport Corporation filename *QE 7312478 D1, 0,065 mA WLB rep.log*
Spectral mismatch correction factor: M = 1.002 ± 0.015

DUT Calibration Procedures:
Newport Corporation document W11 (EQE).docx
Newport Corporation document Area Measurement W12 (Area).docx
Newport Corporation document W13 (IV Sweep).docx

Cal Cert V1.8	Issue Date: Jul 20, 2023	Page 2 of 2
	Reviewed and Approved by: Paulette Frischknecht (Paulette.Frischknecht@mksinst.com)	
This certificate to be reproduced in part only with written permission from the Newport PV Laboratory		

Fig. S18 Photovoltaic Cell Performance Certificate for P-DIP $AgBiS_2$ NCs ink solar cell from Newport.

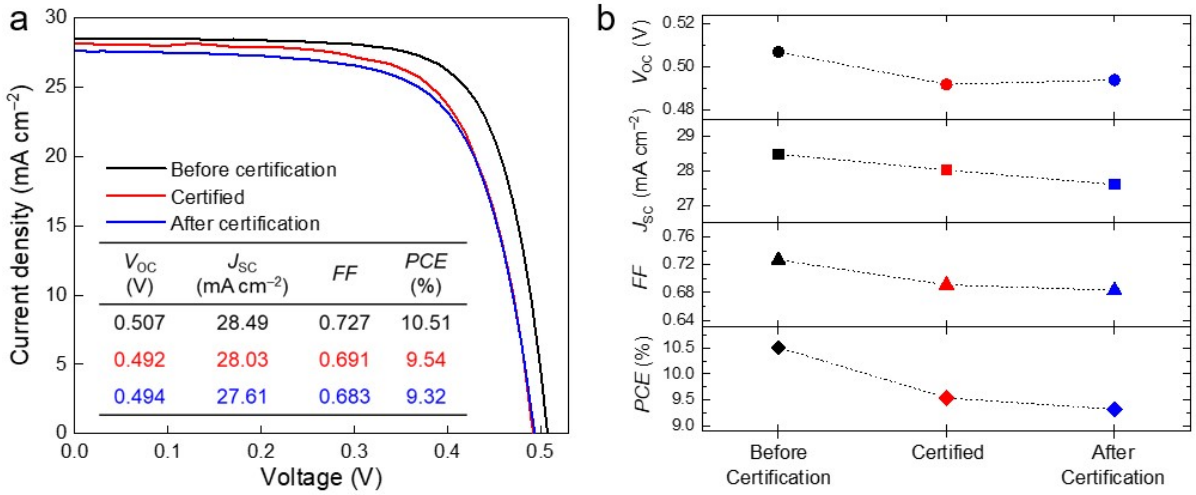

Fig. S19 Performance degradation of P-DIP $AgBiS_2$ NCs ink solar cell during certification process. (a) *J–V* curves measured from identical P-DIP $AgBiS_2$ NCs ink solar cell before (black) and after certification (blue) process comparing with certified efficiency (red) under the forward scan. (b) The variation of measured device parameters before and after certification process (see **Note S3**).

Note S3

We characterized device performance before and after certification process. As shown in **Fig. S19a**, The *PCE* of 10.51% were recorded in our lab before sending device to Newport. However, it was identified that certified *PCE* of the same device, measured under the forward scan, was 9.54% with reduced parameters, notably *FF* loss from 0.73 to 0.69. Moreover, a further decrease in J_{SC} and *FF* was observed in the device measurement after its return to our lab, as summarized in **Fig. S19b.** Based on these results, we carefully assume that deterioration of device during shipping and/or measurement under certification process would be main reasons for degraded parameters of our P-DIP ink device.

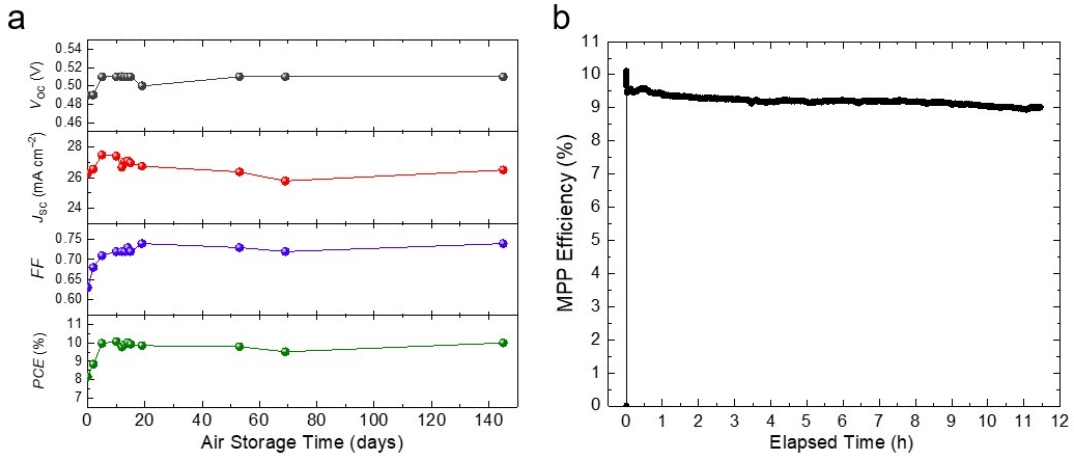

Fig. S20 Device stability of un-encapsulated P-DIP $AgBiS_2$ NCs ink solar cell. (a) Shelf lifetime: The device retained 99.3% of its initial highest *PCE* of 10.1% after 145 days under ambient condition (relative humidity, ~20%, temperature, ~25°C) (b) Operational stability: The device maintained 88.6% of its initial *PCE* of 10.12% after 11h under AM 1.5G 1-sun illumination with fixed forward bias at the maximum power point (MPP) (relative humidity ~60%, temperature, ~25°C).

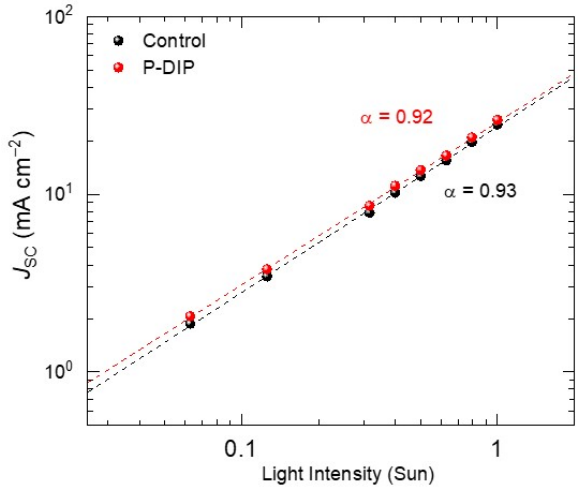

Fig. S21 Light-intensity dependence of J_{SC} characteristic of Control and P-DIP $AgBiS_2$ NCs ink devices.

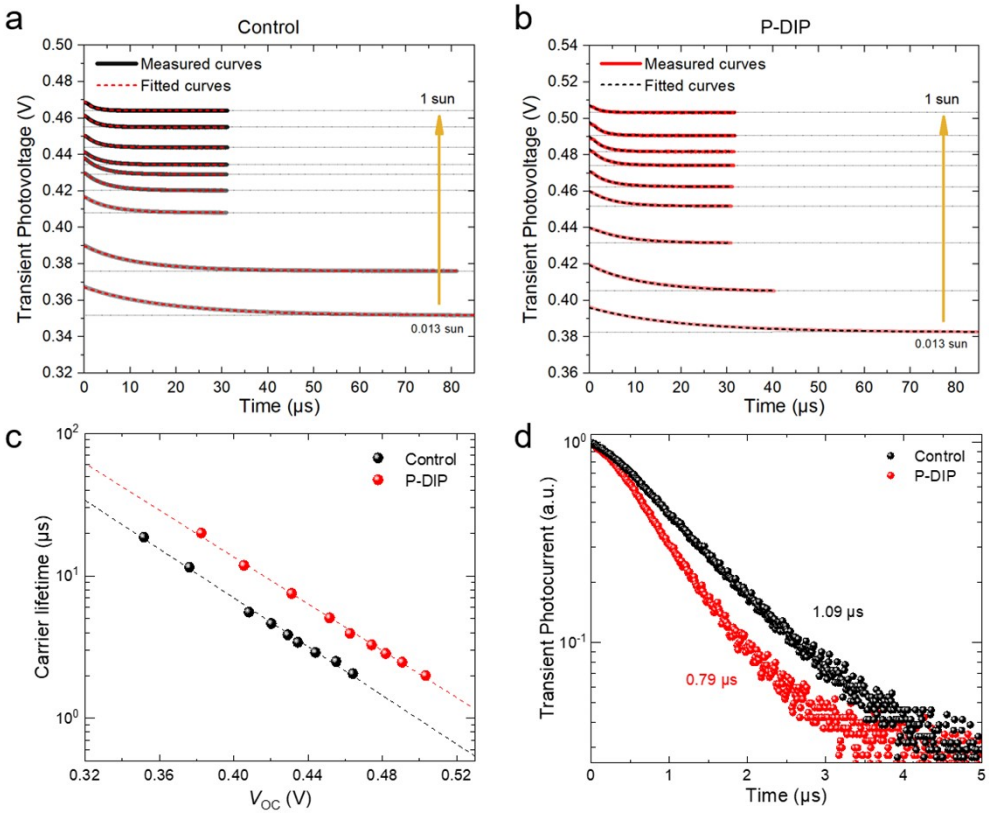

Fig. S22 Investigation of carrier lifetime and extraction capability. TPV analysis of (a) Control (black) and (b) P-DIP (red) $AgBiS_2$ NCs ink devices under varying light intensity condition. (c) Corresponding extracted carrier lifetime. The P-DIP ink device exhibited the improved carrier lifetime at the entire open-circuit conditions, indicating the suppressed nonradiative recombination by synergetic passivation. (d) TPC measurements of Control (black) and P-DIP (red) $AgBiS_2$ NCs ink devices. The faster photocurrent decay lifetime (0.79 μs) was observed in the P-DIP ink device compared to the Control (1.09 μs), demonstrates the improved carrier extraction ability, correlating with J_{SC} improvement in P-DIP ink devices.

Note S4

From TPV and TPC results, the carrier recombination rate (**Fig. 4b**) was determined by dividing the charge density (n) by carrier lifetime under each V_{OC} condition. TPV curves (**Fig. S22a and b**) were fitted with exponential decay to extract carrier lifetimes (**Fig. S22c**). n values were calculated following the equation[11,12]:

$$n = \frac{1}{Aqd}\int_0^{V_{OC}} CdV$$

where, A is the device area, q is the elementary charge, d is the film thickness, and C is the capacitance, evaluated from the $C=\Delta Q/\Delta V_{OC}$ relation. Injected charge (ΔQ) was estimated by integrating TPC plots (**Fig. S22d**). The trap-state density of $AgBiS_2$ NCs ink devices (**Fig. 4c**) was calculated by differentiating n with respect to V_{OC}.

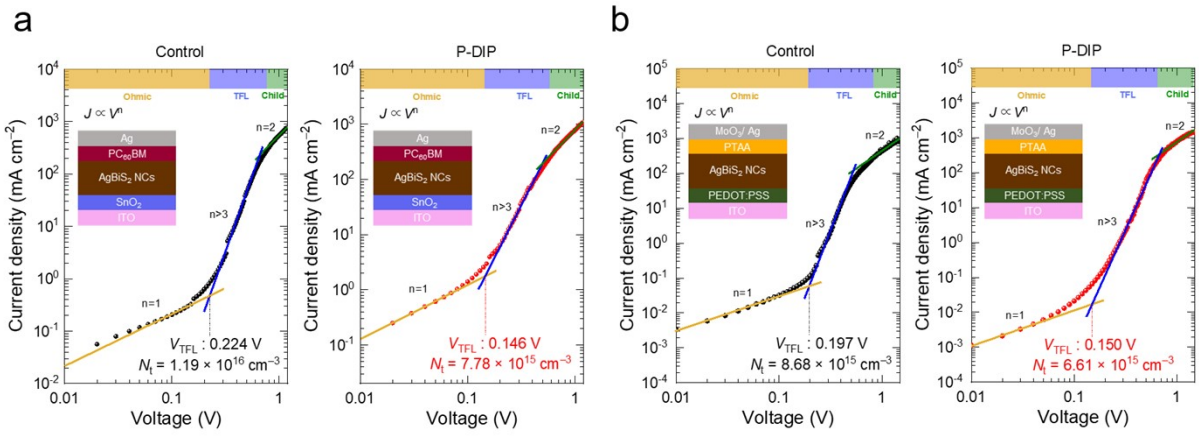

Fig. S23 Estimation of trap density in electron- and hole-only devices Space-charge limited current (SCLC) analysis of (a) electron-, and (b) hole- only device fabricated with Control (black) and P-DIP (red) $AgBiS_2$ NCs inks. As illustrated in the inset schematics, electron- and hole-only devices were constructed with following device configurations: ITO/SnO_2/$AgBiS_2$ NCs films/PCBM/Ag and ITO/PEDOT:PSS/$AgBiS_2$ NCs films/PTAA/MoO_3/Ag, respectively. The trap density (N_t) was calculated from the equation of $N_t = \left(\frac{2\varepsilon\varepsilon_0}{eL^2}\right)V_{TFL}$, where ε is the dielectric constant of $AgBiS_2$[13], ε_0 is the vacuum permittivity, e is the elementary charge, L is the thickness of $AgBiS_2$ NCs film, V_{TFL} is the trap-filled limit voltage.

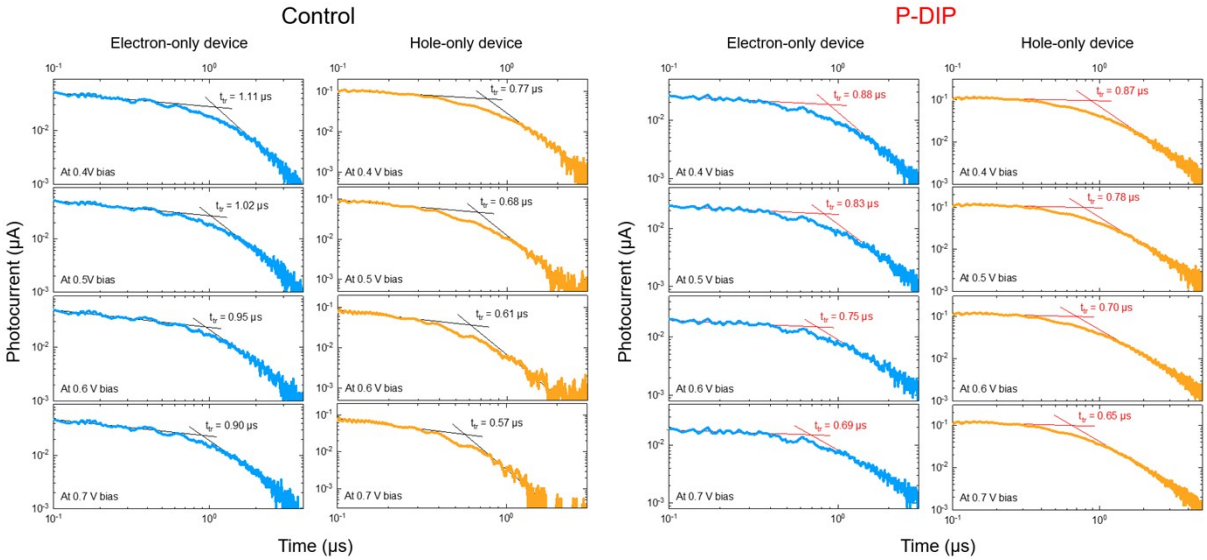

Fig. S24 Time-of-flight (TOF) analysis of electron-(blue) and hole-(orange) only devices of Control and P-DIP ink. Carrier mobility (μ) was calculated using the equation of $\mu = \frac{L^2}{Vt_{tr}}$, where L is the thickness of $AgBiS_2$ NCs film and V is bias voltage, and t_{tr} is the transit time. The extracted t_{tr} under each bias condition was plotted L^2/t_{tr} versus V, as presented in **Fig. 4d** and **e**. Linear fitting was performed to determine the slope of the plot, i.e., μ.

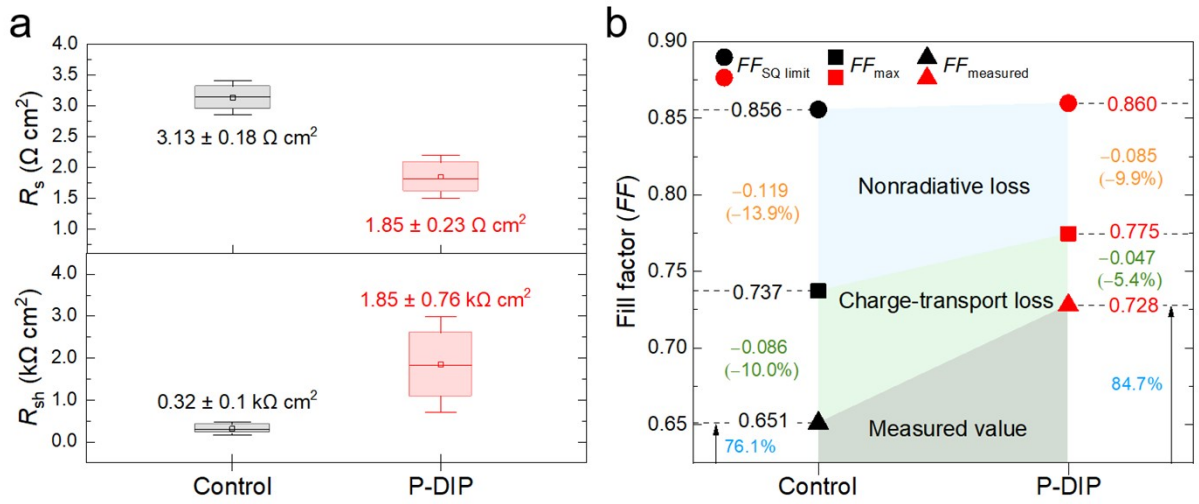

Fig. S25 The effect of synergetic passivation on device resistance and *FF*. (a) Series (R_s) and shunt resistance (R_{sh}) calculated by reciprocal of the slope of fitted straight lines near the V_{OC} for R_s and J_{SC} for R_{sh} derived from each 20 different *J*–*V* curves for Control (black) and P-DIP (red) $AgBiS_2$ NCs solar cells. (b) The *FF* corresponding to Shockley–Queisser limit ($FF_{SQ\ limit}$), maximum *FF* (FF_{max}), and measured *FF* ($FF_{measured}$) for Control (black) and P-DIP (red) $AgBiS_2$ NCs ink solar cells (see **Note S5**). Both nonradiative (bule area) and charge-transport loss (green area) are suppressed in P-DIP ink devices. Furthermore, $FF_{measured}$ of P-DIP ink device reached 94% of its FF_{max}, compared to 88% in Control. This can be attributed to balanced charge transport and extraction in P-DIP ink device.

Note S5

The $FF_{SQ\ limit}$ corresponding to each E_g of Control (1.00 eV) and P-DIP (1.03 eV) $AgBiS_2$ NCs film was acquired utilizing a publicly accessible python-based script. (https://github.com/marcus-cmc/Shockley-Queisser-limit).

Assuming there are no charge transport losses in the device, the FF_{max} can be estimated following the previously reported equation[14]:

$$FF_{Max} = \frac{v_{oc} - ln(v_{oc} + 0.72)}{v_{oc} + 1} \; with \; v_{oc} = \frac{qV_{OC}}{nkT}$$

where, q is the elementary charge, V_{OC} is the open-circuit voltage, n is the ideality factor, k is the Boltzmann constant, and T is the temperature.

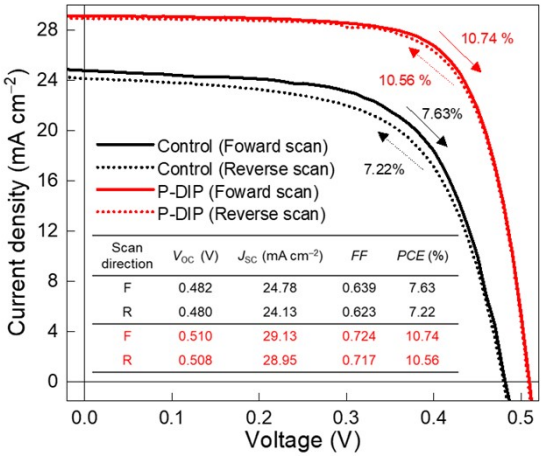

Fig. S26 Device hysteresis. *J–V* curves for Control and P-DIP $AgBiS_2$ NCs solar cells measured under forward and reverse scan. The inset table shows device parameters according to scan directions.

Table S1. Deconvolution parameters of Bi 4*f* XPS spectra measured from Control and P-DIP $AgBiS_2$ NCs ink films.

Spectral Region	Spin-orbit splitting (Δ)	Components	Control			P-DIP		
			Peak Position (eV)	FWHM (eV)	Relative Area (%)	Peak Position (eV)	FWHM (eV)	Relative Area (%)
Bi $4f_{7/2}$	5.3 eV	Bi–S	158.4	0.7	47.5	158.4	0.7	46.9
		Bi–I	159.0	0.7	6.7	159.0	0.7	5.7
		Bi–Cl	-	-	-	159.6	0.7	2.1
		Metallic Bi	157.6	0.7	2.6	157.6	0.7	2.1
Bi $4f_{5/2}$		Bi–S	163.7	0.7	36.1	163.7	0.7	35.6
		Bi–I	164.3	0.7	5.1	164.3	0.7	4.4
		Bi–Cl	-	-	-	164.9	0.7	1.6
		Metallic Bi	162.9	0.7	2.0	162.9	0.7	1.6

Table S2. Deconvolution parameters of S 2*p* XPS spectra measured from Control and P-DIP $AgBiS_2$ NCs ink films.

Spectral Region	Spin-orbit splitting (Δ)	Components	Control			P-DIP		
			Peak Position (eV)	FWHM (eV)	Relative Area (%)	Peak Position (eV)	FWHM (eV)	Relative Area (%)
S $2p_{3/2}$	1.2 eV	$AgBiS_2$	161.3	0.8	65.4	161.3	0.8	55.4
		Bound thiolate (M–SR)	-	-	-	162.3	0.8	11.7
S $2p_{1/2}$		$AgBiS_2$	162.5	0.8	34.6	162.5	0.8	27.1
		Bound thiolate (M–SR)	-	-	-	163.5	0.8	5.8

Table S3. Deconvolution parameters of Cl 2*p* XPS spectra measured from P-DIP $AgBiS_2$ NCs ink films.

Spectral Region	Spin-orbit splitting (Δ)	Components	P-DIP		
			Peak Position (eV)	FWHM (eV)	Relative Area (%)
Cl $2p_{3/2}$	1.6 eV	Metal chloride (M–Cl)	198.2	1.0	25.4
		Alkyl chloride (R–Cl)	200.0	1.0	41.3
Cl $2p_{1/2}$		Metal chloride (M–Cl)	199.8	1.0	12.7
		Alkyl chloride (R–Cl)	201.6	1.0	20.6

Table S4. Deconvolution parameters of O 1*s* spectra measured from Control and P-DIP $AgBiS_2$ NCs ink films.

Spectral Region	Components	Control			P-DIP		
		Peak Position (eV)	FWHM (eV)	Relative Area (%)	Peak Position (eV)	FWHM (eV)	Relative Area (%)
O 1*s*	–OH	532.4	1.7	46.9	532.4	1.7	100
	C–O	533.5	1.7	40.0	-	-	-
	H_2O	535.7	1.7	13.1	-	-	-

Table S5. A summary of reported device parameters for $AgBiS_2$ NCs solar cells, categorized based on ligand-exchange methods and the types of ligands utilized in the device fabrication.

Ligand-exchange method	Types of passivation ligands	V_{OC} (V)	J_{SC} (mA cm^{-2})	*FF*	*PCE* (%)	Certified *PCE* (%)	Year	Ref.
Solid-state	Inorganic	0.50	18.00	0.65	5.84	6.31	2016	[15]
	Inorganic	0.46	22.68	0.61	6.37	-	2020	[16]
	Organic	0.50	27.10	0.68	9.17	8.85	2022	[6]
	Inorganic + Organic	0.47	22.14	0.68	7.07	-	2022	[17]
Solution-phase	Inorganic	0.55	12.41	0.59	4.08	-	2020	[18]
	Organic	0.48	24.90	0.61	7.30	-	2022	[19]
	Inorganic + Organic	0.51	29.15	0.73	10.84	9.36	This work	-

Table S6. Device parameters of P-DIP $AgBiS_2$ NCs devices under different annealing conditions.

Annealing Condition	V_{OC} (V)	J_{SC} (mA cm^{-2})	*FF*	*PCE* (%)
115 °C, 5 min	0.49	25.98	0.66	8.34
130 °C, 2 min	0.49	26.47	0.68	8.76
150 °C, 30 sec	0.50	27.49	0.73	9.98

References

[1] J. R. Durig, X. Zhu and S. Shen, *J. Mol. Struct.*, 2001, **570**, 1.

[2] S. Pavithraa, D. Sahu, G. Seth, J. I. Lo, B. N. Raja Sekhar, B. M. Cheng, A. Das, N. J. Mason and B. Sivaraman, *Astrophys. & Space Sci.*, 2017, **362**, 126.

[3] V. Venkata and K. Venkata Ramiah, *Proc. Indian Acad. Sci.*, 1968, **68**, 109.

[4] M. Acik, T. M. Alam, F. Guo, Y. Ren, B. Lee, R. A. Rosenberg, J. F. Mitchell, I. K. Park, G. Lee and S. B. Darling, *Adv. Energy Mater.*, 2018, **8**, 1701726.

[5] C. Ding, F. Liu, Y. Zhang, S. Hayase, T. Masuda, R. Wang, Y. Zhou, Y. Yao, Z. Zou and Q. Shen, *ACS Energy Lett.*, 2020, **5**, 3224.

[6] Y. Wang, S. R. Kavanagh, I. Burgués-Ceballos, A. Walsh, D. O. Scanlon and G. Konstantatos, *Nat. Photonics*, 2022, **16**, 235.

[7] H. Song, J. Yang, W. H. Jeong, J. Lee, T. H. Lee, J. W. Yoon, H. Lee, A. J. Ramadan, R. D. J. Oliver and S. C. Cho, *Adv. Materials*, 2023, **35**, 2209486.

[8] W. M. J. Franssen, B. J. Bruijnaers, V. H. L. Portengen and A. P. M. Kentgens, *ChemPhysChem.*, 2018, **19**, 3107.

[9] N. K. Noel, M. Congiu, A. J. Ramadan, S. Fearn, D. P. McMeekin, J. B. Patel, M. B. Johnston, B. Wenger and H. J. Snaith, *Joule*, 2017, **1**, 328.

[10] M. Schmid, W. Hieringer, C. H. Schmitz, H.-P. Steinrück, M. Sokolowski and J. M. Gottfried, *J. Phys. Chem. C*, 2011, **115**, 14869.

[11] A. H. Ip, S. M. Thon, S. Hoogland, O. Voznyy, D. Zhitomirsky, R. Debnath, L. Levina, L. R. Rollny, G. H. Carey, A. Fischer, *Nat. Nanotechnol.*, 2012, **7**, 577.

[12] S. Pradhan, A. Stavrinadis, S. Gupta, G. Konstantatos, *ACS Appl. Mater. Interfaces*, 2017, **9**, 27390.

[13] F. Viñes, M. Bernechea and G. Konstantatos, F. Illas, *Phys. Rev. B*, 2016, **94**, 235203.

[14] C. Ding, D. Wang, D. Liu, H. Li, Y. Li, S. Hayase, T. Sogabe, T. Masuda, Y. Zhou and Y. Yao, *Adv. Energy Mater.*, 2022, **12**, 2201676.

[15] M. Bernechea, N. Cates, G. Xercavins, D. So, A. Stavrinadis and G. Konstantatos, *Nat. Photonics*, 2016, **10**, 521.

[16] I. Burgués-Ceballos, Y. Wang, M. Z. Akgul and G. Konstantatos, *Nano Energy*, 2020, **75**, 104961.

[17] C. Kim, I. Kozakci, J. Kim, S. Y. Lee and J. Y. Lee, *Adv. Energy Mater.*, 2022, **12**, 202200262.

[18] S. Y. Bae, J. T. Oh, J. Y. Park, S. R. Ha, J. Choi, H. Choi and Y. Kim, *Chem. Mater.*, 2020, **32**, 10007.

[19] Y. Wang, L. Peng, Z. Wang and G. Konstantatos, *Adv. Energy Mater.*, 2022, **12**, 2200700.